Edge-Enriched MoS$_2$ as a High-Performance Cathode for Aqueous Zn-Ion Batteries

Mengfan Niu,[a] Falian Wan,[a] Wenli Xin,[a] Lei Zhang,[a] Xilin Xiao,[a] Hui Zhang,[a] Zichao Yan,[a, b] and Zhiqiang Zhu*[a, b]

Rechargeable aqueous zinc ion batteries (AZIBs) with the advantages in low cost, high safety, and environmental friendliness have broad application prospects in the field of energy storage. However, the slow diffusion kinetics of multivalent Zn^{2+} in materials make it hard to find a suitable cathode. Herein, HNO$_3$ etched MoS$_2$ with edge-enriched feature is proved to be a promising cathode for high-performance AZIBs. The highly exposed edges with superior electrochemical activity can not only offer more reactive sites for zinc storage but also facilitate electrolyte accessibility and shortens the ion transport pathway, thus accelerating reaction kinetics. As a result, the edge-enriched MoS$_2$ cathode exhibited higher specific capacity of 187 mAhg^{-1} at 0.1 Ag^{-1} and outstanding cycling performance (89% capacity retention after 700 cycles at 1 Ag^{-1}).

Introduction

In the past decades, rechargeable Li-ion batteries (LIBs) has been successfully commercialized and widely used in portable electronic devices and energy storage systems.[1,2] However, the resource limitation of lithium and safety issue of organic electrolytes severely hinder their further development.[3–5] In this regard, aqueous energy storage systems have been considered as promising supports for LIBs, owing to their low-cost, high safety, and considerable ionic conductivity.[6,7] As a classic aqueous battery, aqueous zinc-ion batteries (AZIBs) have received extensive interests due to the resource abundance, low redox potential (−0.763 V), and good environmental tolerance of Zn metal.[8,9] Like LIBs, cathode materials with intercalation mechanisms are generally favored in AZIBs because of their stable crystal structure during ion (de)intercalation process.[10,11] Nonetheless, the strong electrostatic interaction between divalent Zn^{2+} and the cathode materials would lead to sluggish diffusion kinetics of Zn^{2+}, thus resulting in the poor electrochemical performance.[12,13] Therefore, it is desirable to explore suitable cathode materials with alleviated electrostatic interaction to divalent Zn^{2+}.

Up to now, various cathode materials, including vanadium-based oxides,[14,15] manganese-based oxides,[16,17] Prussian blue analogs,[18] and organic compounds[19] have been developed for AZIBs. However, the above materials generally suffered from the limited theoretical capacity and/or the dissolution feature of active content (V and Mn), which would cause structure collapse and capacity fading. In contrast, transition metal dichalcogenides, especially MoS$_2$, have attracted widespread attention because of its adjustable two-dimensional ion transport channels and layer spacing.[20] Nevertheless, the poor conductivity and sluggish diffusion kinetics of Zn^{2+} in the bulk MoS$_2$ interlayers exhibit inferior capacity and rate performance in AZIBs.[21] In regard of this, several effective methods have been proposed to optimize the electrochemical behavior of MoS$_2$ cathode. The phase engineering and interlayer engineering synergy aimed in improving the electronic conductivity and tunning layer spacing of MoS$_2$ has been widely applied to improve the reversible capacity and rate performance of MoS$_2$ cathode.[22–24] However, zinc storage behavior mainly occurs at the edge sites of MoS$_2$, and the inert basal surface of MoS$_2$ greatly limits its capacity.[25] Therefore, designing MoS$_2$ with highly exposed edges is an effective way to provide more active sites for zinc storage. Moreover, edge-enriched structure with shortened ion transport pathways could further improve the ion transport efficiency and reaction kinetics of MoS$_2$ cathode.

Herein, we proposed a nitric acid etching strategy to intentionally construct edge-enriched MoS$_2$ as cathode materials for AZIBs. The strong oxidizing acid can not only corrode the inert basal surface of MoS$_2$ to generate more edge active sites for zinc storage, but also alternate partial electronegative sulfur groups with O atoms, thus promoting the electrolyte accessibility. In addition, the edge exposure degree and the content of O are adjustable by regulating nitric acid concentration (0, 0.01, 0.03, 0.05 M). As expected, the optimized edge-enriched MoS$_2$ cathode with appropriate edge exposure and structure stability exhibited superior specific capacity and rate performance (187 mAhg^{-1} at 0.1 Ag^{-1} and 88 mAhg^{-1} at 5 Ag^{-1}) than that of MoS$_2$ (117 mAhg^{-1} at 0.1 Ag^{-1} and 37 mA hg^{-1} at 5 Ag^{-1}). Our research provides new insights into the design of high performance MoS$_2$ cathode.

[a] M. Niu, F. Wan, W. Xin, L. Zhang, X. Xiao, H. Zhang, Z. Yan, Prof. Z. Zhu
State Key Laboratory of Chemo/Biosensing and Chemometrics, College of Chemistry and Chemical Engineering, Hunan University, Changsha 410082, China
E-mail: zqzhu@hnu.edu.cn

[b] Z. Yan, Prof. Z. Zhu
Greater Bay Area Institute for Innovation, Hunan University, Guangzho 511300, China

Results and Discussion

Figure 1a schematically presents the formation process of edge-enriched MoS_2 nanosheets. The pristine MoS_2 nanosheets was initially synthesized by a hydrothermal reaction at $180\,°C$ for 24 h.[26] The edge-enriched MoS_2 samples were acquired by treating the pristine MoS_2 in different concentration (0.01 M, 0.03 M, 0.05 M) of nitric acid solutions. The obtained sample were denoted as MoS_2-M1, MoS_2-M3, and MoS_2-M5, respectively. The strong oxidizing feature of HNO_3 would corrode the inert basal surface of MoS_2 and introduce O atoms, thus effectively increasing the total number of active sites for zinc storage and shortening the migration path of Zn^{2+}. To investigate the structural evolution of MoS_2 etched in various acid concentrations, the scanning electron microscope (SEM) and transmission electron microscopy (TEM) were performed. As shown in Figure 1b, the pristine MoS_2 shows a typical flower-like structure composed by ultrathin nanosheets. After the acid etching (Figure 1c–e), the shape of nanosheets become rougher, and fractured lattice with decreased size are observed, which would obtain larger specific surface area and more edge sites.[27,28] Figure 1f–i present the high-resolution TEM (HRTEM) images of all samples. Compared with pristine MoS_2, acid-treated MoS_2 with increased HNO_3 concentration exhibit reduced layers, indicating that nitric acid corroded the layer structure and induced the formation of new edges in the structure, thereby increasing the total number of active sites. When the acid concentration increased to 0.05 M, the lattice fragments are observed in MoS_2-M5, implying that overdosed acid would lead to the structure integrity of MoS_2. The MoS_2-M3 with appropriate exposed active sites and intact structure

shows homogeneous distribution of O along with the MoS_2, indicate the successful doping of O atoms under acid etching process (Figure S1, Supporting Information). Additionally, the (002) interlayer spacing of all samples were measured to be ~0.64 nm (Figure S2), demonstrating that the acid etching process did not expand the interlayer spacing of MoS_2.

X-ray diffraction (XRD) was carried out to investigate the effects of nitric acid etching by different concentrations. As shown in Figure 2a, the diffraction peak of pristine MoS_2 at 13.8°, 32.3°, 35.8° and 57.3° are corresponded to the (002), (101), (102) and (110) planes, respectively. And the as-prepared samples are well consistent with the standard MoS_2 (PDF#37-1492), indicating that nitric acid treatment did not generate impurities. Noticeably, there is no significant shift in the (002) peak of MoS_2-M1, MoS_2-M3 and MoS_2-M5, further demonstrating that the acid etching process did not expand the interlayer spacing of MoS_2. It should be noted that the half-peak widths of pristine MoS_2, MoS_2-M1, MoS_2-M3, and MoS_2-M5 are ordered from narrow to wide, implying the smallest grain size of MoS_2-M5 in highest nitric acid concentration. The reduction in grain size may benefit to expose more active edge sites for the treated MoS_2.

Figure 2b shows the Raman spectra of the as-prepared samples. The characteristic peaks of pristine MoS_2 at ~375 and ~406 cm^{-1} are assigned to E^1_{2g} in-plane vibration (Mo—S) modes and A_{1g} out-of-plane vibration (Mo—S), respectively.[29] Compared with pristine MoS_2, the red-shift of A_{1g} peak for acid-treated MoS_2 lead to the decreased distance between the E^1_{2g} and A_{1g} peaks, indicating that acid-treated MoS_2 has smaller size and weaker interlayer interaction.[30,31] To investigate the specific surface area and pore property of the edge-enriched samples,
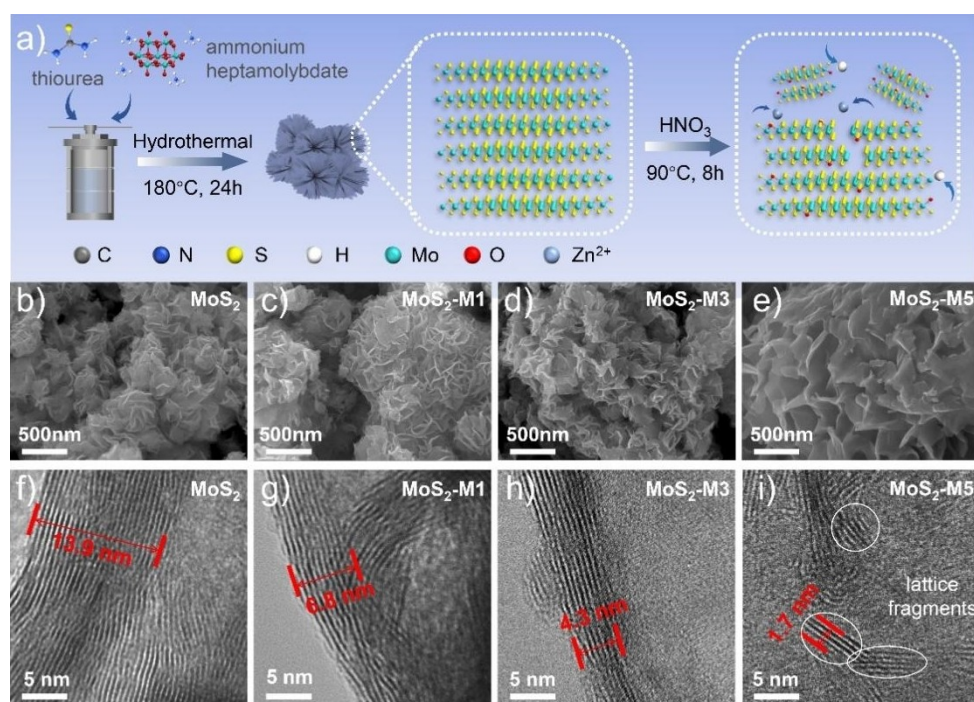

Figure 1. Synthesis and morphology characterization. (a) Illustration of the synthetic process of acid-treated MoS_2. (b–e) SEM images and (f–i) TEM images of MoS_2, MoS_2-M1, MoS_2-M3, and MoS_2-M5.
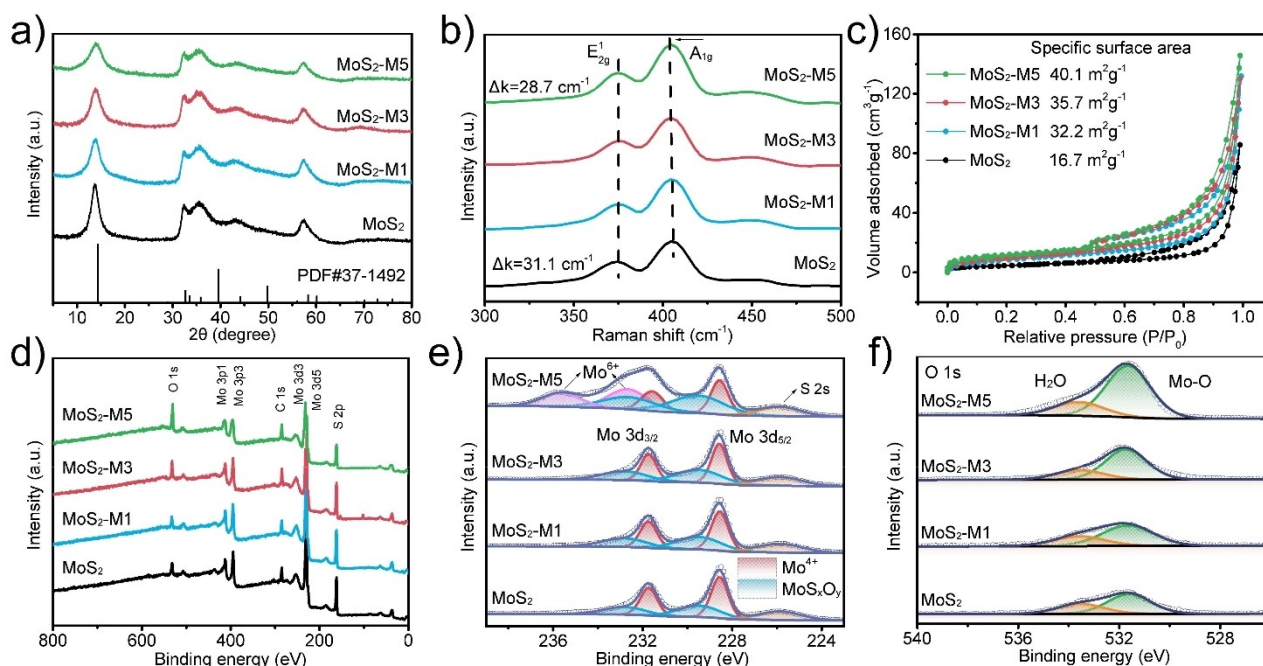
Figure 2. Structural characterization. (a) XRD patterns, (b) Raman spectra, (c) nitrogen adsorption-desorption isothermal curves, (d) XPS survey spectra, (e) Mo 3d and (f) O 1s XPS spectra of MoS_2, MoS_2-M1, MoS_2-M3, and MoS_2-M5.

nitrogen adsorption-desorption measurement was conducted. As shown in Figure 2c, the as-prepared samples are conformed to be H3-type hysteresis loop ranging belonging to type IV isotherms.[32] The BET surface area is calculated to be 16.7 $m^2 g^{-1}$ for pristine MoS_2. With the increase of acid concentration, the surface area of acid-treated MoS_2 gradually increased (32.2 $m^2 g^{-1}$ for MoS_2-M1, 35.7 $m^2 g^{-1}$ for MoS_2-M3 and 40.1 $m^2 g^{-1}$ for MoS_2-M5) with pore sizes of ~4.0 nm (Figure S3). The edge-enriched MoS_2 with enlarged surface area and mesoporous structure is believed to offer facilitate ion transport paths and zinc storage sites.

To further investigate the chemical and electronic states of edge-enriched structure, X-ray photoelectron spectroscopy (XPS) analysis was performed. The XPS survey spectra of all samples shows three characteristic peaks corresponding to Mo, S, and O, respectively (Figure 2d). In the high-resolution Mo 3 d XPS spectra of MoS_2 (Figure 2e), the peaks at low binding energy of 228.5 and 231.7 eV can be ascribed to Mo^{4+} (MoS_2), while the peaks at high binding energy of 229.5 and 232.6 eV are assigned to MoS_xO_y, respectively.[33] Additionally, the proportion of MoS_xO_y gradually enhanced with the increase of HNO_3 concentration. When MoS_2 was etched with 0.05 M nitric acid, the two peaks at 232.6 and 235.6 eV belonging to Mo^{6+} emerged, which may result from the oxidation of Mo^{4+} by HNO_3.[34] As shown in the high-resolution O 1S XPS spectra (Figure 2f), the two double peaks can be assigned to Mo—O bond (531.6 eV) and absorbed H_2O (533.5 eV).[35] It should be noted the ratio of Mo—O bond shows an increased trend along with the acid concentration, which is in line with the results of Mo 3 d XPS spectra, indicating that the acid etching can not only generate more active edge sites but also introduce functional oxygen group.

The electrochemical performance of the as-prepared MoS_2, MoS_2-M1, MoS_2-M3, and MoS_2-M5 cathodes were investigated by CR2032-type coin cells. Figure 3a shows the typical galvanostatic charge/discharge profiles of MoS_2, MoS_2-M1, MoS_2-M3 and MoS_2-M5 at 0.1 $A g^{-1}$. With the increased HNO_3 concentration, MoS_2, MoS_2-M1, MoS_2-M3 and MoS_2-M5 cathode delivered increased specific capacity (117, 150, 187 and 202 $mAh g^{-1}$, respectively), implying that acid-treated MoS_2 with more exposed edges are expect to offer enhanced zinc storage sites. When it comes to rate test, the discharge capacity of MoS_2-M3 varies from 187, 163, 144, 129, 114 to 88 $mAh g^{-1}$ with the increasing current densities from 0.1 to 5 $A g^{-1}$, (Figure 3b and S4a), which is even superior to MoS_2-M5 at high rates. Moreover, when the current density reverted to 0.1 $A g^{-1}$, the specific capacity barely changed, indicating the good reversibility of MoS_2-M3 electrode.

Similar phenomenon can be also observed in cycling performance. As shown in Figure 3c, the MoS_2-M3 electrode achieved a specific capacity of 156 $mAh g^{-1}$ at 0.1 $A g^{-1}$ for 90 cycles, which is higher than that of MoS_2 (120 $mAh g^{-1}$), MoS_2-M1 (140 $mAh g^{-1}$) and MoS_2-M5 (138 $mAh g^{-1}$). When the current density increased to 1 $A g^{-1}$ (Figure 3d), the MoS_2-M5 with more exposed edges exhibited the highest capacity at 1 $A g^{-1}$ in the initial several cycles, while the capacity decayed quickly with 42% capacity retention after 700 cycles. This suggests that the highly concentrated HNO_3 indeed can generate more active sites for zinc storage, while the over-exposed edges may sacrifice the structure integrity of MoS_2.[36,37] In contrast, the sample etched by HNO_3 with lower concentration (0.01 M) displays stable cycling performance but lower capacities, which can be attributed to the limited improvement in the edge sites. The MoS_2-M3 electrode with well-maintained
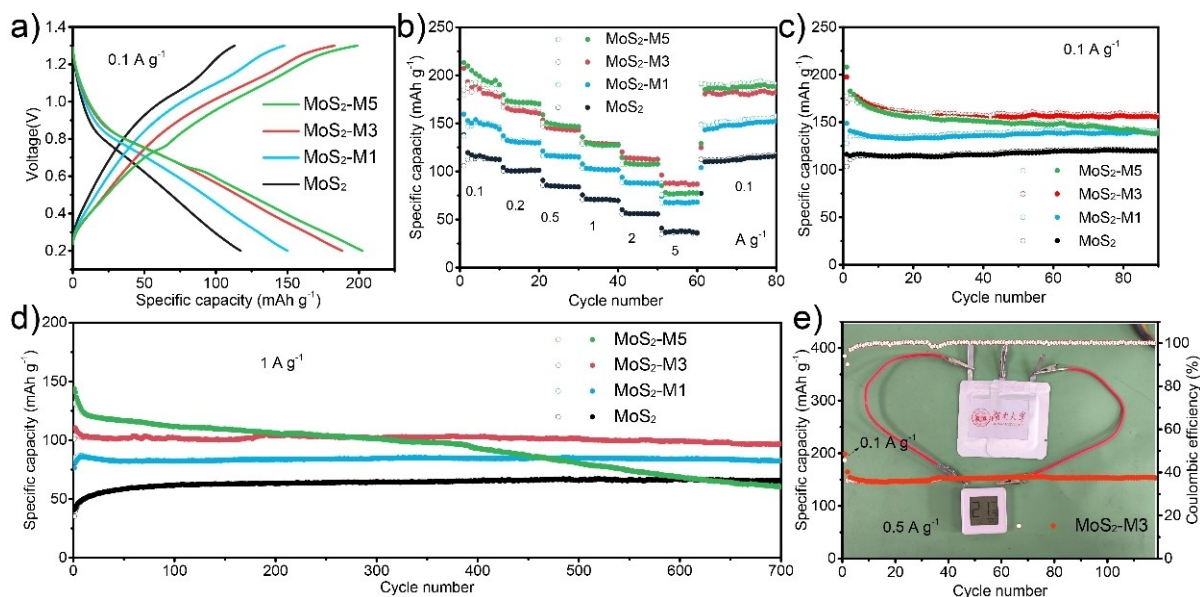
Figure 3. Electrochemical performance. (a) Charge/discharge curves at 0.1 A g^{-1}, (b) rate performances, (c) cycling performances, and (d) long-term cycling stability at 1 A g^{-1} of MoS$_2$, MoS$_2$-M1, MoS$_2$-M3, and MoS$_2$-M5. (e) Cycling performance of the MoS$_2$-M3-based pouch cell at 0.5 A g^{-1}. The inset shows a photograph of the MoS$_2$-M3-based pouch cell powering a thermometer.

charge/discharge curve (Figure S4b) shows the highest specific capacity of 97 mAh g^{-1} after 700 cycles with capacity retention of 89%. As a result, etching with an appropriate concentration of nitric acid is an effective strategy for increasing active sites and maintaining structure integrity, thereby improving capacity and enhancing cycling stability. However, the etching process potentially compromise the structure integrity on the surface of MoS$_2$,[36] thus leading to partial irreversible reaction and, consequently, an initial capacity decay. To evaluate the

practicality of MoS$_2$-M3, pouch cells were assembled by MoS$_2$-M3 cathode, metallic Zn anode, and 3 M Zn(CF$_3$SO$_3$)$_2$ electrolyte. As shown in Figure 3e, the pouch cell exhibited a reversible capacity of ~153 mAh g^{-1} at 0.5 A g^{-1}, with a capacity retention of 98% after 110 cycles. The illuminated thermometer demonstrates the potential of practical applications for MoS$_2$-M3.

To investigate the electrode reaction kinetics, the electrochemical impedance spectroscopy (EIS) of the as-prepared materials (Figure 4a and Table S1) was collected. With increas-
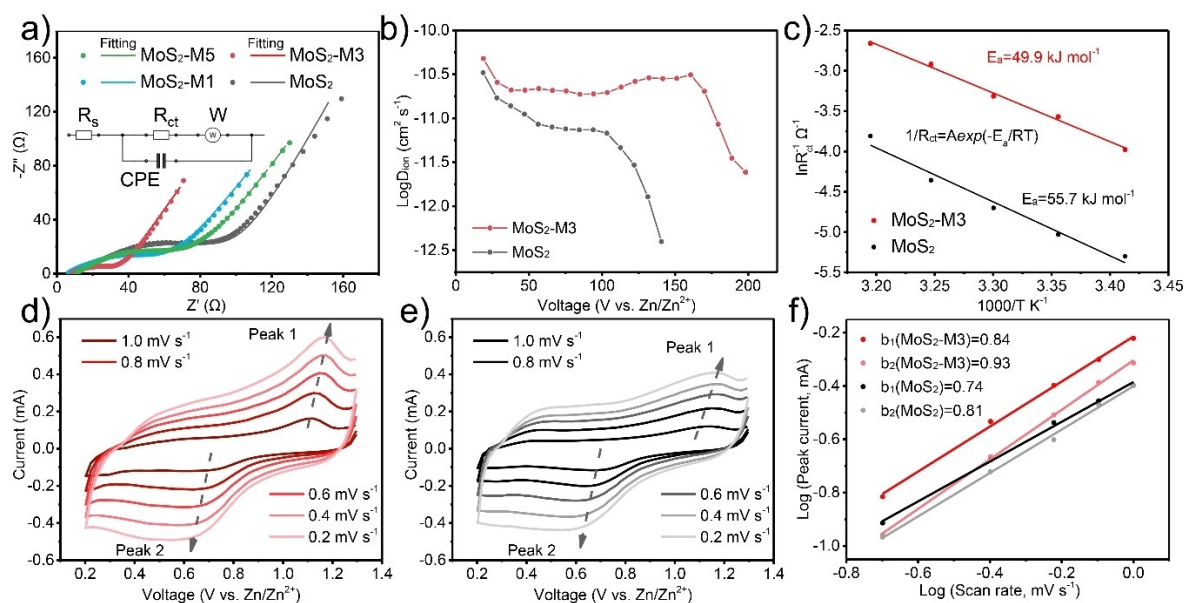

Figure 4. Dynamics characterization. (a) EIS spectra of MoS$_2$, MoS$_2$-M1, MoS$_2$-M3, and MoS$_2$-M5. (b) Ion diffusion coefficients and (c) activation energy of MoS$_2$-M3 and MoS$_2$ electrodes. CV curves of (d) MoS$_2$-M3 and (e) MoS$_2$ electrodes at various scan rates, and the comparison of corresponding b values of (f) MoS$_2$-M3 and MoS$_2$.

Batteries & Supercaps

Research Article
doi.org/10.1002/batt.202400419

Chemistry Europe
European Chemical
Societies Publishing

ing the etching concentration of HNO_3, the charge-transfer resistance (R_{ct}) value of MoS_2 (77.5 Ω), MoS_2-M1 (54.8 Ω) MoS_2-M3 (24.2 Ω) gradually decreased. This trend is because that the generated structure defects during the edge exposing process can optimize the conductivity of MoS_2.[38] When the etching concentration further increases, the R_{ct} value of MoS_2-M5 (62.2 Ω) increases, which should be attributed to the broken 2D electron conjugation by overdosed acid, thus blocking the electron transport along basal surfaces.[39] As displayed in Figure S5, the Warburg coefficients (σ) were calculated based on the equation of $Z' = R_s + R_{ct} + \sigma\omega^{-1/2}$, where ω represents angular frequency. Apparently, the MoS_2-M3 electrode shows the smallest value of σ, reflecting the highest diffusion coefficient of zinc ions (D_{ion}).[40]

Subsequently, we investigated the ion diffusion kinetics of MoS_2-M3 and MoS_2 by galvanostatic intermittent titration technique (GITT). As shown in Figure 4b and Figure S7, the calculated D_{ion} of MoS_2-M3 remained in the range from 10^{-10} to 10^{-11} cm^2 s^{-1}, which is higher than that of pristine MoS_2 (from 10^{-10} to 10^{-12} cm^2 s^{-1}).[41] Furthermore, a detailed analysis of activation energy (E_a) was investigated (Figure S8). The corresponding E_a of MoS_2-M3 and MoS_2 are calculated by the following formula:[42]

$$\frac{1}{R_{ct}} = A\exp\left(-\frac{E_a}{RT}\right) \quad (1)$$

where R_{ct} is the charge transfer impedance, A is a constant, E_a is the activation energy for electrochemical reactions, R is the molar gas constant, and T is the absolute temperature. As shown in Figure 4c, the MoS_2-M3 possesses a E_a of 49.9 kJ mol^{-1}, which is lower than that of pristine MoS_2 (55.7 kJ mol^{-1}). The improved diffusion coefficient and reduced reaction E_a should be related to the easy access of ions by the abundant exposed active edges.

To gain insight into the rapid ion diffusion dynamics of MoS_2-M3, the CV curves of MoS_2 and MoS_2-M3 at different scan sweeps were investigated (Figures 4d–e). The reduction peak at ~0.6 V (Peak 2) correspond to the co-intercalation of H$^+$ and Zn^{2+}, while the oxidation peak (Peak 1) observed at 1.1 V correspond to the co-extraction of H$^+$ and Zn^{2+}.[43] With the increase of the scanning rate from 0.2 to 1.0 mV s^{-1}, the CV curves showed a similar shape, proving the low polarization of MoS_2-M3 electrode. The pseudo-capacitance effect of surface control was studied using the following formula:[44]

$$I = av^b \quad (2)$$

$$\log(i) = b\log(v) + \log(a) \quad (3)$$

where i is the peak current, v is the scan rate, a and b are adjustable parameters. As shown in Figure 4f, the b values of MoS_2 for the redox peaks are 0.74 (b_1) and 0.81 (b_2), which is lower than the value of MoS_2-M3 (0.84 for b_1 and 0.93 for b_2). The higher b values of MoS_2-M3 suggest more pseudocapacitive behavior and therefore lead to high-rate performance. Additionally, the capacitive contribution can be calculated by $i = k_1v + k_2v^{1/2}$ (k_1v and $k_2v^{1/2}$ represent the capacitive process and the

diffusion-controlled process, respectively). The capacitive contribution ratio for MoS_2-M3 progressively improved from 70.4% to 83.8% with increasing scan rate, which is higher than that of MoS_2 (Figure S6). The high pseudocapacitive contribution rate of MoS_2-M3 may originate from its enriched edge sites, which is responsible for the improved specific capacity and superior reaction kinetics.

The reaction mechanism of MoS_2-M3 was further investigated by ex-situ XRD and XPS analysis. Figure 5a shows the initial charge/discharge curve at 0.1 A g^{-1} and the marked states (points A–G) are selected for ex-situ measurements. As shown in Figure 5b, the diffraction peak of (002) plane of MoS_2-M3 exhibits negligible shift, indicating that the interlayer spacing barely expanded during the charging/discharging processes. This phenomenon suggests that the Zn^{2+} storage mechanism for MoS_2-M3 are generally dominated by the exposed edge sites rather than the traditional insertion/extraction behavior in MoS_2.[45] In addition, a peak at ~8° appeared when discharged to 0.6 V, which can be assigned to the emerging of Zn$_x$-(CF$_3$SO$_3$)$_y$(OH)$_{2x-y}$·nH$_2$O (ZFH). When fully discharged to 1.3 V, the intensity of the peak strengthened. During the charge process, the peak of ZFH gradually weakened and disappeared.

This phenomenon can also be observed by XPS analysis. As presented in Figure 5c, there are two obvious peaks from the inserted Zn (1022.6 and 1045.6 eV) and ZFH (1021.1 and 1044.1 eV).[23] And the signals of both Zn and ZFH disappeared when charged back to 1.3 V. This is in good agreement with the SEM images of the MoS_2-M3 electrode at different states (Figures 5d–f). The plate-shaped crystals ZFH were observed in fully discharged state and then disappeared in the fully charged state. The above results implies that the edge-enriched MoS_2 cathode presents a co-storage of H$^+$ and Zn^{2+} in AZIBs.

To further reveal the mechanism of H$^+$/Zn^{2+} co-storage in edge-enriched MoS_2, the MoS_2-M3 electrode was tested in two separate electrolytes: one containing only Zn^{2+} (0.5 M Zn-(CF$_3$SO$_3$)$_2$/AN) and another containing only H$^+$ (0.1 M H$_2$SO$_4$), as presented in Figure S9. In the 0.5 M Zn(CF$_3$SO$_3$)$_2$/AN electrolyte, a discharge capacity of 60 mAh g^{-1} was achieved, which can be attributed to the contribution of Zn^{2+} storage. Similarly, the electrode maintained a discharge capacity of 173 mAh g^{-1} in the 0.1 M H$_2$SO$_4$ electrolyte, attributable to H$^+$ insertion. These results conclusively demonstrate the co-storage mechanism of H$^+$ and Zn^{2+} in the edge-enriched MoS_2.

Conclusions

The edge-enriched MoS_2 for high-performance AZIBs is rationally designed and synthesized via a HNO_3 etching method. The modified MoS_2 with increased exposed edges not only provide more active sites for Zn^{2+} storage but also facilitates easier ions access. Meanwhile, the introduced O group by the strong oxidizing feature of HNO_3 can promote the electrolyte accessibility, thus resulting in higher capacity and fast reaction kinetics. As a result, the edge-enriched MoS_2 electrode in AZIBs presented a high specific capacity of 187 mAh g^{-1} at 0.1 A g^{-1}, excellent rate performance of 88 mAh g^{-1} at 5 A g^{-1}. Moreover,

Batteries & Supercaps

Research Article
doi.org/10.1002/batt.202400419

Chemistry
Europe
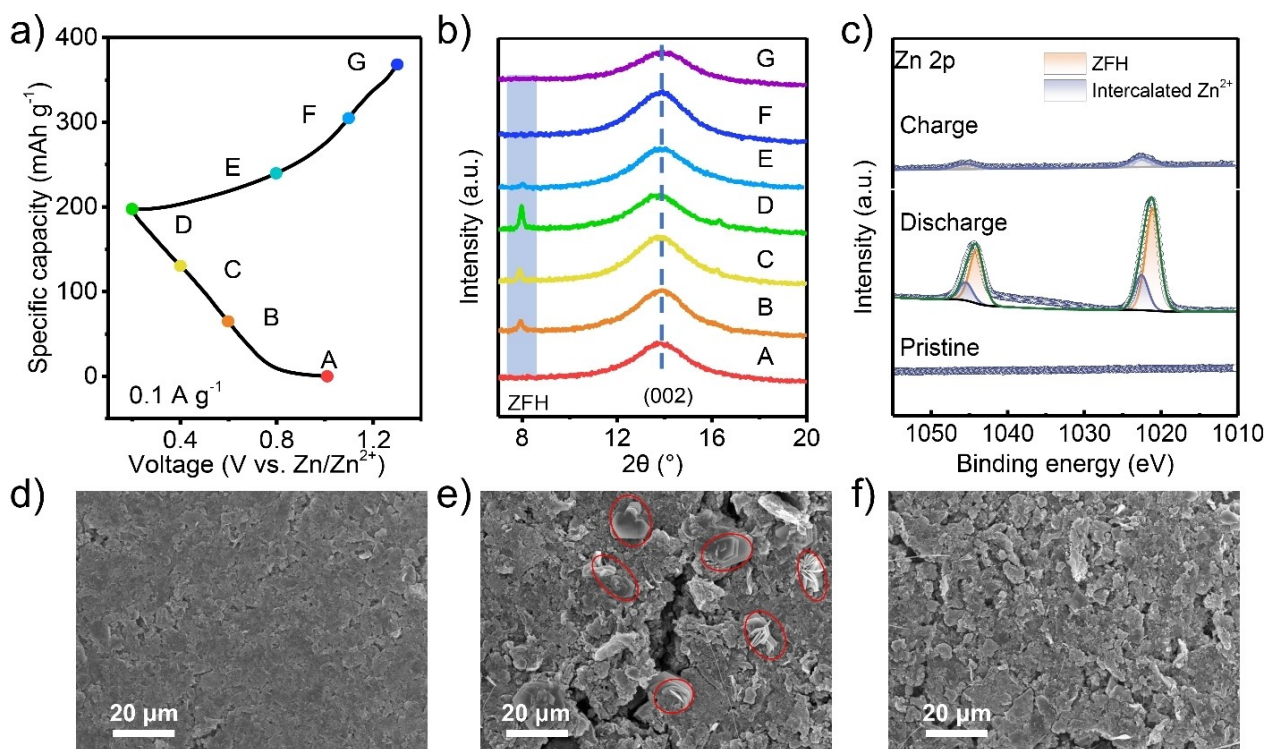European Chemical
Societies Publishing

Figure 5. Reaction mechanism. (a) Initial charge/discharge curve, (b) ex situ XRD patterns, (c) Zn 2p XPS spectra, and corresponding SEM images at (d) original state, (e) discharged state, and (f) charged state of MoS_2-M3 electrode.

the material achieved long-term cyclic stability with 89% capacity retention after 700 cycles at $1\,Ag^{-1}$. Our results emphasize the significance of edge active sites in MoS_2 for efficient zinc storage.

Supporting Information Summary

The authors have cited additional references within the Supporting Information (Ref. [26,46]). Supporting Information is available from the Wiley Online Library or from the author.

Conflict of Interests

The authors declare no conflict of interest.

Data Availability Statement

The data that support the findings of this study are available from the corresponding author upon reasonable request.

[1] Z. Wang, Z. Du, Y. Liu, C. E. Knapp, Y. Dai, J. Li, W. Zhang, R. Chen, F. Guo, W. Zong, X. Gao, J. Zhu, C. Wei, G. He, *eScience* **2023**, *4*, 100189.
[2] Y. Liu, Z. Ma, Z. Yang, Y. Wu, Y. Li, J. Gu, J. Gautam, X. Gong, A. N. Chishti, S. Duan, C. Chen, M. Chen, L. Ni, G. Diao, *Adv. Funct. Mater.* **2022**, *32*, 2109462.
[3] T. Bashir, S. Zhou, S. Yang, S. A. Ismail, T. Ali, H. Wang, J. Zhao, L. Gao, *Electrochem. Energy Rev.* **2023**, *6*, 5.
[4] H. Xia, W. Zhang, S. Cao, X. Chen, *ACS Nano* **2022**, *16*, 8525.
[5] F. Degen, M. Winter, D. Bendig, J. Tübke, *Nat. Energy* **2023**, *8*, 1284.
[6] W. Xin, J. Xiao, J. Li, L. Zhang, H. Peng, Z. Yan, Z. Zhu, *Energy Storage Mater.* **2023**, *56*, 76.
[7] J. Yang, B. Yin, Y. Sun, H. Pan, W. Sun, B. Jia, S. Zhang, T. Ma, *Nano-Micro Lett.* **2022**, *14*, 42.
[8] Y. Tang, J.-H. Li, C.-L. Xu, M. Liu, B. Xiao, P.-F. Wang, *Carbon Neutralization* **2023**, *2*, 186.
[9] X. Chen, W. Li, D. Reed, X. Li, X. Liu, *Electrochem. Energy Rev.* **2023**, *6*, 33.
[10] G. Whang, W. G. Zeier, *ACS Energy Lett.* **2023**, *8*, 5264.
[11] F. Long, J. Shi, Q. Zhang, Z. Liu, Y. Hou, K. Mao, N. Liu, L. Li, F. Long, Y. Gao, *Batteries & Supercaps* **2022**, *5*, 202200110.
[12] Z. Yan, J. Li, H. Liu, H. Zhang, S. Xi, Z. Zhu, *Angew. Chem. Int. Ed.* **2023**, *62*, e202312000.
[13] H. Yao, H. Yu, Y. Zheng, N. W. Li, S. Li, D. Luan, X. W. Lou, L. Yu, *Angew. Chem. Int. Ed.* **2023**, *62*, e202315257.
[14] Y. Cui, Y. Ding, L. Guo, C. Guo, Y. Liu, Y. Bai, G. Li, K. Wang, *Energy Mater.* **2023**, *3*, 300023.
[15] X. Dou, X. Xie, S. Liang, G. Fang, *Sci. Bull.* **2024**, *69*, 833.

[16] S. Guo, L. Qin, J. Wu, Z. Liu, Y. Huang, Y. Xie, G. Fang, S. Liang, *Natl. Sci. Rev.* **2024**, *11*, nwae181.

[17] Y. Hu, Z. Liu, L. Li, S. Guo, X. Xie, Z. Luo, G. Fang, S. Liang, *Natl. Sci. Rev.* **2023**, *10*, nwad220.

[18] G. Yang, Z. Liang, Q. Li, Y. Li, F. Tian, C. Wang, *ACS Energy Lett.* **2023**, *8*, 4085.

[19] W. Gou, T. Jiang, W. Wang, Q. Fan, Y. Zhang, *Chin. Chem. Lett.* **2023**, *34*, 107760.

[20] M. I. A. Abdel Maksoud, A. G. Bedir, M. Bekhit, M. M. Abouelela, R. A. Fahim, A. S. Awed, S. Y. Attia, S. M. Kassem, M. A. Elkodous, G. S. El-Sayyad, S. G. Mohamed, A. I. Osman, A. H. Al-Muhtaseb, D. W. Rooney, *Environ. Chem. Lett.* **2021**, *19*, 3645.

[21] C. W. Kang, J. Park, G. H. Kim, K. C. Ko, S. U. Son, *ACS Appl. Mater. Interfaces* **2023**, *15*, 7887.

[22] S. Gao, S. Chen, F. Shi, W. Jiang, J. Chen, *J. Power Sources* **2024**, *591*, 233866.

[23] S. Li, X. Zhao, T. Wang, J. Wu, X. Xu, P. Li, X. Ji, H. Hou, X. Qu, L. Jiao, Y. Liu, *Angew. Chem. Int. Ed.* **2024**, *136*, e202320075.

[24] F. Li, H. Ma, H. Sheng, Z. Wang, Y. Qi, D. Wan, M. Shao, J. Yuan, W. Li, K. Wang, E. Xie, W. Lan, *Small* **2024**, *20*, 2306276.

[25] S. Li, Y. Liu, X. Zhao, K. Cui, Q. Shen, P. Li, X. Qu, L. Jiao, *Angew. Chem. Int. Ed.* **2021**, *60*, 20286.

[26] Y. Ma, D. Leng, X. Zhang, J. Fu, C. Pi, Y. Zheng, B. Gao, X. Li, N. Li, P. K. Chu, Y. Luo, K. Huo, *Small* **2022**, *18*, 2203173.

[27] W. Zhang, Z. Xie, X. Wu, M. Sun, X. Deng, C. Liu, Z. Liu, Q. Huang, *Mater. Lett.* **2018**, *230*, 232.

[28] L. Zhao, Y. Xiong, X. Wang, R. Zhao, X. Chi, Y. Zhou, H. Wang, Z. Yang, Y. Yan, *Small* **2022**, *18*, 2106939.

[29] Y. Shi, Y. Zhou, D.-R. Yang, W.-X. Xu, C. Wang, F.-B. Wang, J.-J. Xu, X.-H. Xia, H.-Y. Chen, *J. Am. Chem. Soc.* **2017**, *139*, 15479.

[30] C. Lee, H. Yan, L. E. Brus, T. F. Heinz, J. Hone, S. Ryu, *ACS Nano* **2010**, *4*, 2695.

[31] Y. Liang, H. D. Yoo, Y. Li, J. Shuai, H. A. Calderon, F. C. Robles Hernandez, L. C. Grabow, Y. Yao, *Nano Lett.* **2015**, *15*, 2194.

[32] C. Li, C. Liu, Y. Wang, Y. Lu, L. Zhu, T. Sun, *Energy Storage Mater.* **2022**, *49*, 144.

[33] H. Liang, Z. Cao, F. Ming, W. Zhang, D. H. Anjum, Y. Cui, L. Cavallo, H. N. Alshareef, *Nano Lett.* **2019**, *19*, 3199.

[34] W. Xu, Q. Fang, D. Liu, K. Zhang, M. Habib, C. Wu, X. Zheng, H. Liu, S. Chen, L. Song, *Molecules* **2016**, *21*, 1318.

[35] L. Jiang, Y.-J. Zhang, X.-H. Luo, L. Yu, H.-X. Li, Y.-J. Li, *Chem. Eng. J.* **2021**, *425*, 130611.

[36] F. Liu, Z. Fan, *Chem. Soc. Rev.* **2023**, *52*, 1723.

[37] N. Luo, C. Chen, D. Yang, W. Hu, F. Dong, *Appl. Catal. B* **2021**, *299*, 120664.

[38] R. Sun, S. Dong, J. Yang, J. Xiong, C. Wang, S. Lu, Y. Zhang, H. Fan, *Chem. Commun.* **2023**, *59*, 1845.

[39] J. Xie, J. Zhang, S. Li, F. Grote, X. Zhang, H. Zhang, R. Wang, Y. Lei, B. Pan, Y. Xie, *J. Am. Chem. Soc.* **2013**, *135*, 17881.

[40] Z. Yao, W. Zhang, X. Ren, Y. Yin, Y. Zhao, Z. Ren, Y. Sun, Q. Lei, J. Wang, L. Wang, T. Ji, P. Huai, W. Wen, X. Li, D. Zhu, R. Tai, *ACS Nano* **2022**, *18*, 12095.

[41] W. Zhang, H. Xia, Z. Zhu, Z. Lv, S. Cao, J. Wei, Y. Luo, Y. Xiao, L. Liu, X. Chen, *CCS Chem.* **2020**, *3*, 1245.

[42] M. Yang, Z. Yan, J. Xiao, W. Xin, L. Zhang, H. Peng, Y. Geng, J. Li, Y. Wang, L. Liu, Z. Zhu, *Angew. Chem. Int. Ed.* **2022**, *61*, e202212666.

[43] F. Shao, F. Huang, X. Wang, Z. Li, X. Huang, W. Huang, L. Dong, F. Kang, W. Liu, C. Xu, *Chem. Eng. J.* **2022**, *448*, 137688.

[44] J. Wang, J. Polleux, J. Lim, B. Dunn, *J. Phys. Chem. C* **2007**, *111*, 14925.

[45] W. Xu, C. Sun, K. Zhao, X. Cheng, S. Rawal, Y. Xu, Y. Wang, *Energy Storage Mater.* **2019**, *16*, 527.

[46] H. Geng, M. Cheng, B. Wang, Y. Yang, Y. Zhang, C. C. Li, *Adv. Funct. Mater.* **2020**, *30*, 1907684.